Solar-wind electron precipitation on weakly magnetized bodies: The planet Mercury

Federico Lavorenti[1,2], Pierre Henri[1,3], Francesco Califano[2], Jan Deca[4,5,6], Simon Lindsay[7], Sae Aizawa[8,2,9], and Johannes Benkhoff[10]

[1] Laboratoire Lagrange, OCA, UCA, CNRS, 96 Bd de l'Observatoire, 06304 Nice, France
  e-mail: `federico.lavorenti@oca.eu`
[2] Dipartimento di Fisica "E. Fermi", Univ. di Pisa, L.go Bruno Pontecorvo 3, 56127 Pisa, Italy
[3] LPC2E, CNRS, Univ. d'Orléans, OSUC, CNES, 3 Av. de la Recherche Scientifique, 45071 Orléans, France
[4] LASP, Univ. of Colorado Boulder, 1234 Innovation Drive Boulder, CO 80303, USA
[5] IMPACT, NASA/SSERVI, 3400 Marine St., Boulder, CO 80303, USA
[6] LATMOS, UVSQ, 11 Bd D'Alembert, 78280 Guyancourt, France
[7] School of Physics & Astronomy, University of Leicester, University Rd LE1 7RH, Leicester, UK
[8] IRAP, UPS, CNRS, CNES, 9 Av. du Colonel Roche, 31028 Toulouse, France
[9] JAXA, 3-1-1 Yoshinodai, Chuo-ku, Sagamihara-shi, Kanagawa, Japan
[10] ESA/ESTEC, Keplerlaan 1, 2200 AG Noordwijk, The Netherlands

ABSTRACT

Rocky objects in the Solar System (such as planets, asteroids, moons, and comets) undergo a complex interaction with the flow of magnetized, supersonic plasma emitted from the Sun called solar wind. We address the interaction of such a flow with the planet Mercury, considered here as the archetype of a weakly magnetized, airless, telluric body immersed in the solar wind. Due to the lack of dense atmosphere, a considerable fraction of solar-wind particles precipitate on Mercury. The interaction processes between precipitating electrons and other nonionized parts of the system remain poorly understood. Shading light on such processes is the goal of this work. Using a 3D fully kinetic self-consistent plasma model, we show for the first time that solar-wind electron precipitation drives (i) efficient ionization of multiple neutral exosphere species and (ii) emission of X-rays from the surface of the planet. We conclude that, compared to photoionization, electron-impact ionization should not be considered a secondary process for the H, He, O, and Mn exosphere. Moreover, we provide the first, independent evidence of X-ray aurora-like emission on Mercury using a numerical approach.

Key words. planets and satellites: magnetic fields – plasmas – X-rays: general – planets and satellites: aurorae – solar wind – planet-star interactions

1. Introduction

The planet Mercury is a nearby example of a rocky, weakly magnetized body immersed in the solar-wind plasma. Mercury's environment presents an ideal scenario to better understand the physics governing the interaction between solid bodies (such as telluric planets, moons, asteroids, and comets) and the solar wind. Mercury's ionized environment is nonetheless intrinsically nonlinear and hard to understand. Such complexity is due (i) to the strong coupling between the plasma and the planet's magnetosphere, exosphere, and surface and (ii) to the strongly kinetic dynamics of the ions in such a small magnetosphere (5% the size of Earth's magnetosphere). At present, the physical processes controlling the electron interactions in the system are a scientific enigma, with underlying roots ranging from plasma to solid-state physics (Milillo et al. 2010). As an example, electron acceleration in the magnetosphere is thought to be at the origin of X-ray aurora-like emission from the surface of Mercury. However, on the one hand, this hypothesis remains to be confirmed, and on the other, the dependence of such a process on the upstream solar-wind conditions remains unknown.

The Sun acts as an external energy driver, sustaining the dynamics at Mercury. Solar radiation and particles are the source (via desorption and sputtering) and sink (via radiation pressure and ionization) of the neutral exosphere surrounding Mercury, respectively. Moreover, the solar-wind plasma considerably alters the shape of Mercury's magnetic field. The intrinsic magnetic field generates a scaled-down, Earth-like magnetosphere able to partially shield the planet's surface from the impinging solar wind. Part of the solar wind enters the magnetosphere, interacts with Mercury's magnetic field and, given the absence of an atmosphere, precipitates down to the planet surface. Studying this plasma precipitation is key to our understanding of the strong coupling between Mercury's magnetosphere, exosphere, and surface, and of coupling of this kind around weakly magnetized bodies in general.

To date, only two missions (Mariner 10 and MESSENGER) have been devoted to the exploration of Mercury's environment. Mariner 10 provided the first electron observations, showing electron fluxes in the range ~20–600 eV throughout the magnetosphere (Ogilvie et al. 1977). Sporadic bursts above tens of keV were also detected (Wurz & Blomberg 2001, and references

Table 1. Common numerical parameters of RunN and RunS with purely northward and southward IMF, respectively.

Box dimensions	(L_x, L_y, L_z)		$(-9{:}+6,\pm6,\pm6)\,R$
Number of cells	(N_x, N_y, N_z)		$(960,768,768)$
Spatial resolution	$(\mathrm{d}x, \mathrm{d}y, \mathrm{d}z)$		$0.015\,R$
Time resolution	$\mathrm{d}t$		1.4 ms
Macro-particles per cell [a]	PPC		128
Solar-wind number flux	$\mathcal{F}_{\mathrm{sw}}$	$n_{\mathrm{sw}} V_{\mathrm{sw}}$	$1.2 \times 10^9\,1\,\mathrm{cm}^{-2}\,\mathrm{s}^{-1}$
Solar-wind energy flux	$\mathcal{E}_{\mathrm{sw}}$	$T_{e,\mathrm{sw}} n_{\mathrm{sw}} V_{\mathrm{sw}}$	$2.4 \times 10^{10}\,\mathrm{eV}\,\mathrm{cm}^{-2}\,\mathrm{s}^{-1}$
Ion-to-electron mass ratio	$m_{\mathrm{i}}/m_{\mathrm{e}}$		100
Light-to-Alfvén speed ratio	$c/V_{\mathrm{A,i}}$	$c\sqrt{4\pi n_{\mathrm{sw}}}/B_{\mathrm{sw}}$	188
Planet-to-gyro radius ratio	R/ρ_{i}	$R \cdot B_{\mathrm{sw}} e/c \sqrt{m_{\mathrm{i}} T_{\mathrm{i,sw}}}$	10

Notes. [a]Total number of macro-particles, ions plus electrons.

therein). MESSENGER (Solomon et al. 2007) could not measure the core of the electron distribution function, but it provided direct observations of high-energy electrons above 35 keV (Ho et al. 2011, 2012) and indirect observations of suprathermal electrons in the range ∼1–10 keV (Lawrence et al. 2015; Baker et al. 2016; Dewey et al. 2018; Ho et al. 2016). MESSENGER also reported the first evidence of electron-induced X-ray emissions from the surface (Lindsay et al. 2016, 2022). These missions provided a novel but still fragmented picture of the solar-wind electron interaction with Mercury and weakly magnetized bodies in general. In the near future, the joint ESA/JAXA space mission BepiColombo (Benkhoff et al. 2021) will revolutionize our understanding of Mercury's environment thanks to (i) its two-satellite composition and (ii) its instrumental payload with resolution down to electron kinetic scales (Milillo et al. 2020). BepiColombo will observe the whole electron (Saito et al. 2021; Huovelin et al. 2020) and X-ray (Bunce et al. 2020) spectrum with unprecedented resolution. This will allow better constraint of the current hypothesis on the electron motion in the system and exploration, for the first time, of the kinetic plasma dynamics at subion scales. However, the complexity of these measurements is such that only through global models, including the electron dynamics, can the true potential of these measurements be unveiled. Here, we present such a model, and use it to interpret the fragmented picture left by past MESSENGER observations, while paving the way for the future BepiColombo ones.

In the past, global numerical models of Mercury's interaction with the solar wind have focused on the ion dynamics (Kallio & Janhunen 2003; Trávníček et al. 2010; Richer et al. 2012; Fatemi et al. 2020). Such models included the ion kinetic physics self-consistently, but neglected the kinetic physics of electrons (treated as a massless neutralizing fluid). Those models neglect electron acceleration processes and therefore also their feedback on the magnetosphere and surface. Previous studies that did model electron trajectories prescribed constant electromagnetic fields (i.e., a test-particle approach; Schriver et al. 2011a; Walsh et al. 2013), but this completely neglects the feedback of electron physics on the large-scale global evolution. Nonetheless, Schriver et al. (2011a) provided a first estimate of electron precipitation maps at Mercury, but their results did not address the energy distribution of electrons at the surface (due to the small statistical sample of test electrons). To overcome these limitations, in this work we study the precipitation of electrons on Mercury-like bodies using a global, fully kinetic model. Our model includes the electron dynamics self-consistently from the large, planet scale down to the electron gyro-radius.

We assess electron precipitation at the surface of Mercury under purely northward and southward solar-wind conditions. Our numerical results are then used to compute (i) the electron impact ionization rates in Mercury's low-altitude exosphere, and (ii) the X-ray photon emission profiles from Mercury's surface. This novel, self-consistent approach provides (i) the first estimate of the efficiency of electron impact ionization – a process usually neglected in exosphere models – for multiple exospheric species, and (ii) the first estimate of the X-ray luminosity of a rocky, weakly magnetized body driven by solar-wind electron precipitation.

2. Methods

2.1. Three-dimensional fully-kinetic global plasma simulations

We use the semi-implicit particle-in-cell code iPIC3D, which solves the Vlasov–Maxwell system of equations in a three-dimensional Cartesian box by discretizing the ion and electron distribution function (Markidis et al. 2010). The simulation setup includes (i) a uniform solar-wind plasma composed of two oppositely charged species (ions and electrons with a normalized mass of $m_{\mathrm{i}} = 1$ and $m_{\mathrm{e}} = 1/100$, respectively) injected from the sunward side of the box and (ii) a scaled-down model of the planet Mercury with radius $R = 230$ km (radius reduced by around a factor 10 from its real value) and magnetic dipole moment $200\ nT/R^3$. The dipole field is shifted northward by $0.2\,R$ in agreement with the MESSENGER magnetic field observations (Anderson et al. 2012). A scaled-down planet enables us to run a global, fully kinetic simulation on present state-of-the-art computing facilities. Scaling-down the planet but keeping the good ordering of physical spatial and temporal scales preserves the global magnetosphere structure and dynamics (Lavorenti et al. 2022). Analogous planet-rescaling techniques have been used to run global simulations of Mercury using a hybrid code on past-decade computing facilities (Trávníček et al. 2007, 2009, 2010) in support to MESSENGER observations. On top of that, we adopt $m_{\mathrm{i}}/m_{\mathrm{e}}$ and $c/V_{\mathrm{A,i}}$ rescaling techniques (see Table 1), a procedure commonly used in fully kinetic simulations in order to target kinetic processes using manageable computational resources (Bret & Dieckmann 2010; Le et al. 2013; Lavorenti et al. 2021). The artificially increased electron mass adopted here is responsible for a reduced electron thermal speed in the solar wind (here 460 km s^{-1} instead of the realistic value 1970 km s^{-1}). However, this reduction does not alter the thermal energy of solar-wind electrons and preserves a value of the electron Mach number in the solar wind of smaller than one (here 0.87 instead

of 0.20). To reduce the ratio $c/V_{A,i}$ (equal to $\omega_{p,i}/\omega_{c,i}$), we artificially reduce the light speed c in the simulations. This reduction would severely affect the electromagnetic modes with $\omega/k \approx c$, but these are not included in our model. We further discuss the impact of these rescalings in Appendix A. At the box boundaries, the outermost cells are populated with solar-wind plasma and the electromagnetic fields are linearly smoothed to their solar-wind values. Inside the planet, macro-particles are removed using a charge-balanced scheme (Lavorenti et al. 2022). We initialize the simulations with a solar-wind density of $n_{sw} = 30\,cm^{-3}$, a speed of $V_{sw} = 400\,km\,s^{-1}$ in the Sun–planet direction, a magnetic field amplitude of $B_{sw} = 20\,nT$, and temperature of $T_{i,sw} = T_{e,sw} = 21.5\,eV$. Two different simulation setups are used, with purely northward (RunN) or southward (RunS) interplanetary magnetic field (IMF). These two IMF setups, not designed to be the most statistically significant at Mercury, are used to grasp the physics of interest in the system under a simplified geometry (see James et al. (2017) for a statistical analysis of the IMF at Mercury). This simulation setup was validated by Lavorenti et al. (2022), who compared the large-scale structure of Mercury's magnetosphere with the mean structure observed by MESSENGER. The numerical parameters employed in our two runs are reported in Table 1.

2.2. How to link plasma precipitation to exosphere and surface processes?

To compute electron impact ionization (EII) rates and X-ray fluorescence (XRF) emissions, we employ (i) the electron energy distribution at the surface $f_e(\phi, \theta, E)$ computed from our fully kinetic simulations and (ii) reference cross sections $\sigma_X(E)$ found in the literature. Hereafter, ϕ and θ are the geographical longitude and latitude, respectively, and E is the electron energy. To compute the EII rates of H, He, Na, Mg, Al, Si, K, and Mn, we use the analytical formula provided by Golyatina & Maiorov (2021); for O we use the NIST tool by Kim et al. (2005); and for Ca we use the curve in Zatsarinny et al. (2019, Fig. 8 therein). XRF cross sections are obtained using the NIST tool by Llovet et al. (2014). The rate of a given process (EII or XRF with a given atomic species) is:

$$\nu_X(\phi, \theta) = \int_0^\infty f_e(\phi, \theta, E)\sigma_X(E)\sqrt{\frac{2E}{m_e}}\,dE. \quad (1)$$

This quantity measures the typical interaction time $\tau_X = 1/\nu_X$ of the electron flux with one target atom at one point of the surface, and is independent of the number of target atoms. For this reason, the EII rates computed from Eq. (1) do not depend on the spatial distribution of exospheric neutral atoms. In Eq. (1), we use the physical electron mass m_e at the denominator to compute the rate in SI units.

To compute the X-ray flux emitted from the surface, information on surface density and composition are needed. Using Mercury's mean geochemical surface composition derived from MESSENGER observations (McCoy et al. 2018, Table 7.1 therein) and assuming a mean surface mass density of $3\,g\,cm^{-3}$, we obtain the number density n_s of the most abundant surface species (namely O, Na, Mg, Al, Si, S, Ca and Fe). We also assume an electron penetration depth $\delta = 1\,\mu m$. The total X-ray photon flux as a function of longitude, latitude is:

$$\mathcal{F}_{XRF}(\phi, \theta) = \sum_s F_{XRF,s}(\phi, \theta) = \delta \sum_s \nu_{XRF,s}(\phi, \theta)n_s, \quad (2)$$
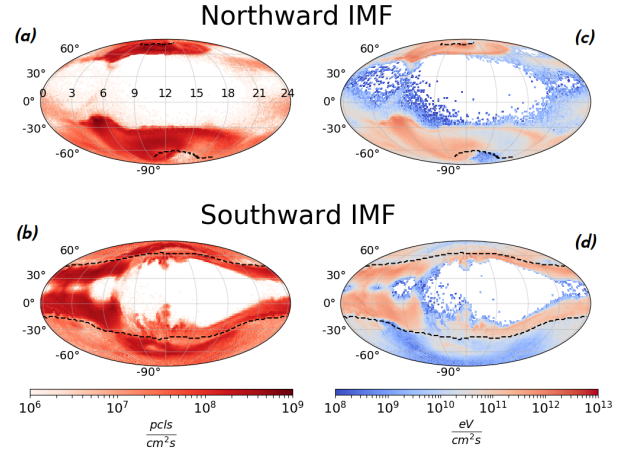

Fig. 1. Electron precipitation maps at the surface of Mercury using Mollweide projection. Panels a and b show the number fluxes in units of electrons $cm^{-2}\,s$. Panels c and d show the energy fluxes in units of $eV\,cm^{-2}\,s$. The vertical axis corresponds to geographical latitude and the horizontal axis corresponds to local time (as indicated in panel a, 12 is the subsolar longitude). Dashed black lines show the boundary between open and closed magnetic field lines (i.e., the cusps).

where $\nu_{XRF,s}$ is computed using Eq. (1). The emitted photon flux per species $F_{XRF,s}$ is proportional to both n_s and δ. Therefore, variations in the value of these two quantities, such as spatial variations on the surface between regions with different compositions, can be directly linked to variations in the emitted X-ray flux.

3. Results

3.1. Properties of electron precipitation on the planet's surface

In both simulations, the global system reaches a quasi-steady state after a time $T \approx 10\,s$. This timescale T is comparable to the Dungey cycle period in our scaled-down Mercury. In our model, scaling down the magnetosphere size by a factor 10 corresponds to scaling down the Dungey cycle period from $\approx 2\,min$ to $\approx 10\,s$. Starting from this time T, we integrate the plasma precipitation on the planet's surface for a time interval $\Delta t = 50\,ms$, corresponding to about two electron gyro-periods ($\tau_{ce} = 2\pi/\omega_{ce} = 30\,ms$ in our simulations with the chosen electron mass rescaling). From the precipitated plasma, we compute the electron precipitation maps shown in Fig. 1. Moreover, solar-wind ion precipitation maps in the same format as Fig. 1 can be found in Appendix B. The precipitation maps are obtained using a total of $\sim 10^6$ macro-particles, enabling a good representation of the electron energy distribution function at the surface. Data concerning the macro-particles collected onto the surface are publicly available at this link[1].

The electron precipitation maps in Fig. 1 show significant spatial inhomogeneities for both explored IMF configurations. In the case of northward IMF (RunN), the solar-wind electrons are (i) energized up to energies of a few keV and (ii) concentrated onto the northern and southern cusps. In RunN, the northern cusp extends down to a latitude of $\sim+60°$ while the southern cusp extends to a latitude of $\sim-30°$. Such north–south asymmetry is due to the northward shift of the planetary magnetic dipole. Energy fluxes in the cusps reach values of $\sim 10^{12}\,eV\,cm^{-2}\,s$, two

---

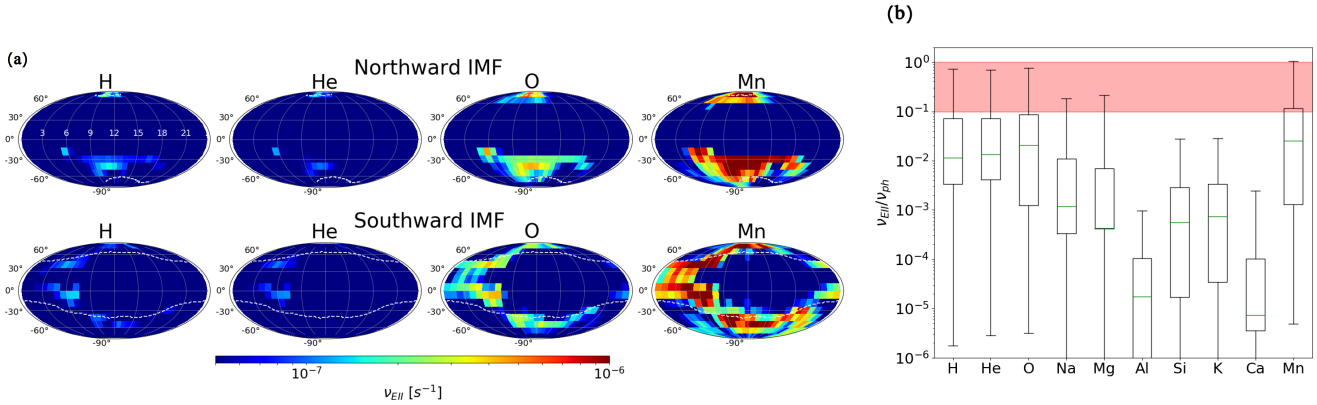[1] https://doi.org/10.5281/zenodo.7589891

Fig. 2. Electron impact ionization rates in Mercury's exosphere. Panel a: maps in the same format as Fig. 1 of EII rates of exosphere H, He, O, and Mn. Panel b: box-plot of the distribution of EII-to-photoionization frequency ratios for multiple exosphere species (RunN and RunS are merged). The red box highlights the region of significant EII rates.

orders of magnitude higher than in the pristine solar wind (see Table 1). In the case of southward IMF (RunS), high-energy electrons (up to few keV) precipitate at low latitudes close to the magnetic equator (from $-50°$ to $+60°$) and mainly at the nightside. This energy flux is higher on the dawn side (LT 0–6 h) than on the dusk side (LT 18–24 h), in agreement with indirect electron observations by MESSENGER (Baker et al. 2016; Dewey et al. 2018; Lindsay et al. 2016). Possible drivers of such an electron enhancement at dawn are (i) the dawn-ward drift of electrons injected from the neutral line in the tail toward the planet (Christon 1987; Dong et al. 2019; Lavorenti et al. 2022) and (ii) the enhanced magnetic reconnection at dawn in the plasma sheet (Sun et al. 2022a, Chap. 4 therein). In RunS, low-energy electrons (around tens of eV) precipitate around the northern and southern poles. These electrons precipitate directly from the solar wind onto the surface without crossing the reconnection region.

We find that 1.5 times more electrons precipitate on the surface in RunS than in RunN. The rate of precipitating electrons is 1.7×10^{25} s^{-1} (2.6×10^{25} s^{-1}) in RunN (RunS), corresponding to an effective area of 2% (3%) of the total 4π planet surface area. The rates, fluxes, and energies reported here are in agreement with the findings of Schriver et al. (2011a). For unmagnetized bodies (such as Mars, Venus, comets, or the Moon), the effective area exposed to solar wind is 50% of the body's surface area given the absence of any magnetic field shielding. In those cases, precipitation is much higher as compared to Mercury, but the solar wind does not suffer acceleration in the magnetosphere (Kallio et al. 2008). A weak magnetic field, like that of Mercury, therefore (i) filters the solar-wind in precise regions of the surface and (ii) accelerates the incoming electrons by around a factor 100 in energy. Both effects (filtering and acceleration) are not possible around unmagnetized objects.

3.2. Interaction of precipitating electrons with the exosphere and surface

Before hitting the rocky surface of the planet, electrons interact with the exosphere. We address the efficiency of electron impact ionization (EII) of multiple exosphere species using the electron energy distribution from our simulations, because we want to assess the relevance of EII (usually considered a secondary, negligible effect) in comparison to photoionization (the primary ionization process). The distribution of EII rates computed from

Eq. (1) over the planet's surface is shown in Fig. 2a for hydrogen (H), helium (He), oxygen (O), and manganese (Mn) for both simulation runs. Moreover, maps of EII rates for all exosphere species considered in this work can be found in Appendix C in the same format as Fig. 2a. These four species have the highest EII-to-photoionization frequency ratio, as shown in Fig. 2b (photoionization rates ν_{ph} are taken from Huebner & Mukherjee (2015) for quiet sun conditions and rescaled to Mercury's aphelion). For H, He, O, and Mn, EII is relevant (i) in the dayside, where locally $\nu_{EII} \approx \nu_{ph}$ and (ii) in the nightside, where ionization of neutrals is dominated by EII with typical rates of ~$0.1 \nu_{ph}$. Differently from photoionization, EII is (i) localized on specific regions of the surface and (ii) strongly dependent on the upstream solar-wind parameters, as shown in Fig. 2a. Variations in the IMF direction, such as moving from northward to southward IMF, induce strong variations in EII rates locally at the surface. We also show that EII of sodium (Na), magnesium (Mg), aluminum (Al), silicon (Si), potassium (K), and calcium (Ca) are negligible under nominal solar-wind conditions, as shown in Fig. 2b. This result supports the common assumption of negligible EII for the Na exosphere (Sun et al. 2022b; Jasinski et al. 2021). Nevertheless, compared to photoionization, EII should not be considered a secondary process for the H, He, O, and Mn exosphere.

When hitting the surface, electrons induce the emission of photons from the surface atoms via X-ray fluorescence (XRF). This latter is driven by electrons with energies above a few hundred eV (Bunce et al. 2020, Table 5 therein). From the electron energy distribution at the surface obtained from our simulations, we compute the flux of emitted X-rays $\mathcal{F}_{XRF}$ from Eq. (2), as shown in Fig. 3a. We include XRF emission from the most abundant species on Mercury's surface, namely O, Na, Mg, Al, Si, S, Ca, and Fe. Figure 3b shows the relative intensity of each of the X-ray emission lines from these different elements. We find that electron-induced X-ray emissions from the surface of Mercury present strong spatial inhomogeneities dependent upon the upstream IMF conditions. Regions of strongest X-ray emission correspond to regions of high-energy electron precipitation, namely the poles (in the case of northward IMF) and the low-latitude, dawn–midnight sector (in the case of southward IMF). In these regions, the emitted X-ray flux reaches values of the order of 10^7 photons cm^{-2} s^{-1} (mostly coming from the O-Kα line). The MESSENGER/XRS instrument was able to measure X-rays from Si- and Ca-group ions at Mercury's
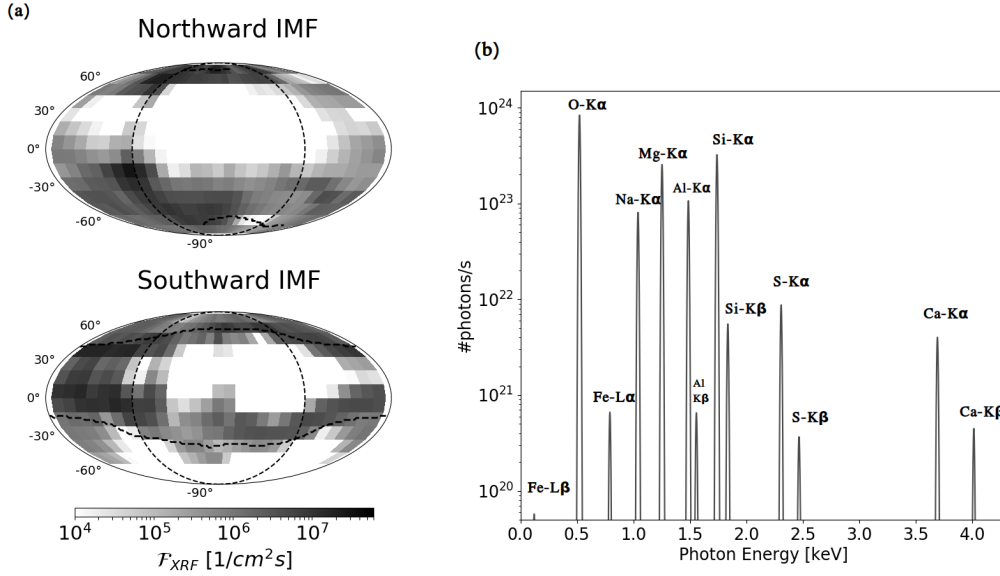
Fig. 3. X-ray emissions from the surface of Mercury induced from high-energy electron precipitation. Panel a: maps (same format as Fig. 1) showing the total X-ray photon flux emitted from the surface in our two runs, as computed in Eq. (2). Panel b: INTENSITY of the different X-ray emission lines considered in this study. The intensity of these lines corresponds to the surface integral of the X-ray photon flux $F_{XRF,s}$ in Eq. (2). To better visualize the lines, a Gaussian profile with a width of 5 eV is used.

nightside (Lindsay et al. 2016), and partially at the dayside (Lindsay et al. 2022) during periods of low solar activity. Due to limited energy range and energy resolution, XRS was not able to measure the rich variety of emission lines obtained from our simulations shown in Fig. 3b. Our results corroborate the idea – built upon MESSENGER observations – that Mercury's X-ray aurora-like emission is due to high-energy electron precipitation at the surface. Moreover, our modeled X-ray flux provides a new means to interpret and plan future in situ observations by the BepiColombo/MIXS instrument (Bunce et al. 2020). The integrated X-ray luminosity of Mercury from electron-induced XRF is $\mathcal{L} \approx 10^{24}$ photons s^{-1}. Such luminosity is comparable to that of other Solar System bodies shining in X-rays (Bhardwaj et al. 2007), such as comets, Jupiter, and Saturn. Nonetheless, remote observations from Earth of Mercury's X-ray aurora remain challenging due to the strong background of X-ray photons coming from the Sun.

4. Conclusions

To conclude, using a novel, fully kinetic 3D approach, we investigated the properties of solar-wind electron precipitation on the surface of Mercury-like bodies. The magnetosphere of those bodies acts (i) as a shield, allowing only a few percent of the solar wind to precipitate onto the surface and (ii) as an accelerator, increasing electron energies by a factor $\sim$100. Using the self-consistently modeled electron precipitation fluxes as the input to exosphere and surface impact processes, we find two main results.

First, electron impact ionization of exospheric H, He, O, and Mn at Mercury is shown to be an efficient process. On the dayside, electron impact ionization is locally as efficient as photoionization. On the nightside, it is the dominant source of ionization of neutrals because photoionization is inhibited. The ionization rates provided here are crucial to complement fluid and hybrid models of Mercury's environment, which cannot model electron acceleration processes.

Second, electrons accelerated in the magnetosphere induce X-ray emission from the surface with fluxes of the order

of 10^7 photons cm^{-2} s^{-1}, mostly from surface oxygen. This result corroborates and provides the physical origin of the X-ray aurora-like emissions observed by the MESSENGER/XRS instrument; it also paves the way for the future planning of BepiColombo/MIXS observations.

References

Aizawa, S., Delcourt, D., Terada, N., & André, N. 2020, Planet. Space Sci., 193, 105079
Anderson, B. J., Johnson, C. L., Korth, H., et al. 2012, J. Geophys. Res. (Planets), 117, E00L12
Arró, G., Califano, F., & Lapenta, G. 2022, A&A, 668, A33
Bacchini, F., Pucci, F., Malara, F., & Lapenta, G. 2022, Phys. Rev. Lett., 128, 025101
Baker, D. N., Dewey, R. M., Lawrence, D. J., et al. 2016, J. Geophys. Res. (Space Phys.), 121, 2171
Benkhoff, J., Murakami, G., Baumjohann, W., et al. 2021, Space Sci. Rev., 217, 90
Bhardwaj, A., Elsner, R. F., Randall Gladstone, G., et al. 2007, Planet. Space Sci., 55, 1135
Bret, A., & Dieckmann, M. E. 2010, Phys. Plasmas, 17, 032109
Bunce, E. J., Martindale, A., Lindsay, S., et al. 2020, Space Sci. Rev., 216, 126
Christon, S. P. 1987, Icarus, 71, 448
Deca, J., Divin, A., Henri, P., et al. 2017, Phys. Rev. Lett., 118, 205101
Deca, J., Divin, A., Lue, C., Ahmadi, T., & Horányi, M. 2018, Commun. Phys., 1, 12

Deca, J., Henri, P., Divin, A., et al. 2019, Phys. Rev. Lett., 123, 055101
Dewey, R. M., Raines, J. M., Sun, W., Slavin, J. A., & Poh, G. 2018, Geophys. Res. Lett., 45, 10,110
Dibraccio, G. A., Slavin, J. A., Boardsen, S. A., et al. 2013, J. Geophys. Res. (Space Phys.), 118, 997
Dong, C., Wang, L., Hakim, A., et al. 2019, Geophys. Res. Lett., 46, 11,584
Dungey, J. W. 1961, Phys. Rev. Lett., 6, 47
Exner, W., Heyner, D., Liuzzo, L., et al. 2018, Planet. Space Sci., 153, 89
Fatemi, S., Poirier, N., Holmström, M., et al. 2018, A&A, 614, A132
Fatemi, S., Poppe, A. R., & Barabash, S. 2020, J. Geophys. Res. (Space Phys.), 125, e27706
Golyatina, R. I., & Maiorov, S. A. 2021, Atoms, 9, 90
Grošelj, D., Mallet, A., Loureiro, N. F., & Jenko, F. 2018, Phys. Rev. Lett., 120, 105101
Haggerty, C. C., Shay, M. A., Drake, J. F., Phan, T. D., & McHugh, C. T. 2015, Geophys. Res. Lett., 42, 9657
Herčík, D., Trávníček, P. M., Johnson, J. R., Kim, E.-H., & Hellinger, P. 2013, J. Geophys. Res. (Space Phys.), 118, 405
Herčík, D., Trávníček, P. M., Å tverák, Å. t., & Hellinger, P. 2016, J. Geophys. Res. (Space Phys.), 121, 413
Hesse, M., Schindler, K., Birn, J., & Kuznetsova, M. 1999, Phys. Plasmas, 6, 1781
Ho, G. C., Krimigis, S. M., Gold, R. E., et al. 2011, Science, 333, 1865
Ho, G. C., Krimigis, S. M., Gold, R. E., et al. 2012, J. Geophys. Res.: Space Phys., 117
Ho, G. C., Starr, R. D., Krimigis, S. M., et al. 2016, Geophys. Res. Lett., 43, 550
Huebner, W., & Mukherjee, J. 2015, Planet. Space Sci., 106, 11
Huovelin, J., Vainio, R., Kilpua, E., et al. 2020, Space Sci. Rev., 216, 94
James, M., Imber, S. M., Bunce, E. J., et al. 2017, J. Geophys. Res.: Space Phys., 122, 7907
Jasinski, J. M., Cassidy, T. A., Raines, J. M., et al. 2021, Geophys. Res. Lett., 48, e92980
Kallio, E., & Janhunen, P. 2003, Ann. Geophys., 21, 2133
Kallio, E., Wurz, P., Killen, R., et al. 2008, Planet. Space Sci., 56, 1506
Karimabadi, H., Roytershteyn, V., Wan, M., et al. 2013, Phys. Plasmas, 20, 012303
Kim, Y.-K., Irikura, K. K., Rudd, M. E., et al. 2005, Electron-Impact Ionization Cross Section for Ionization and Excitation Database, Version 3.0 (National Institute of Standards and Technology, Gaithersburg, Maryland)
Lapenta, G., Pucci, F., Goldman, M. V., & Newman, D. L. 2020, ApJ, 888, 104
Lavorenti, F., Henri, P., Califano, F., Aizawa, S., & André, N. 2021, A&A, 652, A20
Lavorenti, F., Henri, P., Califano, F., et al. 2022, A&A, 664, A133
Lawrence, D. J., Anderson, B. J., Baker, D. N., et al. 2015, J. Geophys. Res. (Space Phys.), 120, 2851
Le, A., Egedal, J., Ohia, O., et al. 2013, Phys. Rev. Lett., 110, 135004
Lindsay, S. T., James, M. K., Bunce, E. J., et al. 2016, Planet. Space Sci., 125, 72
Lindsay, S. T., Bunce, E. J., Imber, S. M., et al. 2022, J. Geophys. Res. (Space Phys.), 127, e29675
Llovet, X., Salvat, F., Bote, D., et al. 2014, NIST Database of Cross Sections for Inner-Shell Ionization by Electron or Positron Impact, Version 1.0 (Gaithersburg, Maryland: National Institute of Standards and Technology)

Markidis, S., Lapenta, G., & Rizwan-uddin 2010, Math. Comput. Simul., 80, 1509
McCoy, T. J., Peplowski, P. N., McCubbin, F. M., & Weider, S. Z. 2018, The Geochemical and Mineralogical Diversity of Mercury, eds. S. C. Solomon, L. R. Nittler, & B. J. Anderson, Cambridge Planetary Science (Cambridge University Press), 176
Milillo, A., Fujimoto, M., Kallio, E., et al. 2010, Planet. Space Sci., 58, 40
Milillo, A., Fujimoto, M., Murakami, G., et al. 2020, Space Sci. Rev., 216, 93
Ogilvie, K. W., Scudder, J. D., Vasyliunas, V. M., Hartle, R. E., & Siscoe, G. L. 1977, J. Geophys. Res., 82, 1807
Olshevsky, V., Servidio, S., Pucci, F., Primavera, L., & Lapenta, G. 2018, ApJ, 860, 11
Omidi, N., Blanco-Cano, X., Russell, C. T., & Karimabadi, H. 2004, Adv. Space Res., 33, 1996
Parashar, T. N., & Gary, S. P. 2019, ApJ, 882, 29
Parashar, T. N., Matthaeus, W. H., Shay, M. A., & Wan, M. 2015a, ApJ, 811, 112
Parashar, T. N., Salem, C., Wicks, R. T., et al. 2015b, J. Plasma Phys., 81, 905810513
Parashar, T. N., Matthaeus, W. H., & Shay, M. A. 2018, ApJ, 864, L21
Pezzi, O., Liang, H., Juno, J. L., et al. 2021, MNRAS, 505, 4857
Pucci, F., Matthaeus, W. H., Chasapis, A., et al. 2018, ApJ, 867, 10
Richer, E., Modolo, R., Chanteur, G. M., Hess, S., & Leblanc, F. 2012, J. Geophys. Res. (Space Phys.), 117, A10228
Roytershteyn, V., Boldyrev, S., Delzanno, G. L., et al. 2019, ApJ, 870, 103
Saito, S., & Nariyuki, Y. 2014, Phys. Plasmas, 21, 042303
Saito, Y., Delcourt, D., Hirahara, M., et al. 2021, Space Sci. Rev., 217, 70
Schriver, D., Trávníček, P., Ashour-Abdalla, M., et al. 2011a, Planet. Space Sci., 59, 2026
Schriver, D., Trávníček, P. M., Anderson, B. J., et al. 2011b, Geophys. Res. Lett., 38
Shay, M. A., & Drake, J. F. 1998, Geophys. Res. Lett., 25, 3759
Slavin, J. A., Lepping, R. P., Wu, C.-C., et al. 2010, Geophys. Res. Lett., 37, L02105
Solomon, S. C., McNutt, R. L., Gold, R. E., & Domingue, D. L. 2007, Space Sci. Rev., 131, 3
Sun, W., Dewey, R. M., Aizawa, S., et al. 2022a, Sci. China Earth Sci., 65, 25
Sun, W., Slavin, J. A., Milillo, A., et al. 2022b, J. Geophys. Res. (Space Phys.), 127, e30280
Tóth, G., Chen, Y., Gombosi, T. I., et al. 2017, J. Geophys. Res.: Space Phys., 122, 10,336
Trávníček, P., Hellinger, P., & Schriver, D. 2007, Geophys. Res. Lett., 34, L05104
Trávníček, P. M., Hellinger, P., Schriver, D., et al. 2009, Geophys. Res. Lett., 36, L07104
Trávníček, P. M., Schriver, D., Hellinger, P., et al. 2010, Icarus, 209, 11
Vega, C., Roytershteyn, V., Delzanno, G. L., & Boldyrev, S. 2020, ApJ, 893, L10
Verscharen, D., Parashar, T. N., Gary, S. P., & Klein, K. G. 2020, MNRAS, 494, 2905
Walsh, B. M., Ryou, A. S., Sibeck, D. G., & Alexeev, I. I. 2013, J. Geophys. Res. (Space Phys.), 118, 1992
Wurz, P., & Blomberg, L. 2001, Planet. Space Sci., 49, 1643
Zatsarinny, O., Parker, H., & Bartschat, K. 2019, Phys. Rev. A, 99, 012706

Appendix A: Fully kinetic simulations: Impact of rescaling

In our fully-kinetic simulations, we rescale the ion-to-electron mass ratio m_i/m_e, the plasma-to-cyclotron frequency ratio ω_{pi}/ω_{ci}, and the normalized planet radius R in order to be able to run the simulations on state-of-the-art HPC facilities while maintaining a good scale separation between electron, ion, and planetary scales. We are confident that the use of such rescaled parameters does not qualitatively alter the physical processes at play in our simulations.

On state-of-the-art HPC facilities, computational constraints impose the use of rescaled parameters to run fully kinetic simulations of large systems, such as Mercury's magnetosphere. If such rescalings are done "carefully", the modeled environment is still representative of the real one to a good degree of approximation, as demonstrated by the large number of publications for similar systems using reduced parameters. The exact meaning of "carefully" strongly depends on the plasma process under consideration. In the following, we address the impact of each of the rescaled parameters on the simulation results. In Sect. A.1, we show how the rescalings of m_i/m_e and ω_{pi}/ω_{ci} affect the microphysics in fully kinetic simulations while leaving the large-scale structure unchanged. In Sect. A.2, we discuss the role of a reduced planet radius on the results of global plasma simulations of planetary systems.

A.1. Effects of m_i/m_e and ω_{pi}/ω_{ci} on the microphysics

Fully kinetic simulations of space plasmas are commonly performed using (i) a reduced mass ratio m_i/m_e of the order of $25 - 400$ (Karimabadi et al. 2013; Deca et al. 2017, 2018; Pucci et al. 2018; Parashar et al. 2018; Olshevsky et al. 2018; Deca et al. 2019; Lapenta et al. 2020; Vega et al. 2020; Pezzi et al. 2021; Bacchini et al. 2022; Arró et al. 2022; Lavorenti et al. 2022) instead of the real hydrogen proton-to-electrom mass ratio of 1836, and (ii) a reduced ω_{pi}/ω_{ci} ratio of the order of 10–500 (Karimabadi et al. 2013; Saito & Nariyuki 2014; Parashar et al. 2015b,a; Grošelj et al. 2018; Parashar & Gary 2019; Royter-shteyn et al. 2019) instead of more realistic values of the order of 10^3–10^4 found typically in the solar wind. These two choices allow one to reduce the computational time needed to simulate a system of a given size. Indeed, the computational time of a fully kinetic simulation with fixed system size, grid resolution $dx \sim d_e$, time step $dt \sim \omega_{pe}^{-1}$, and time $T \sim \omega_{ci}^{-1}$ scales as:

$$T_{comp} \sim \left(\frac{\omega_{pi}}{\omega_{ci}}\right)\left(\frac{m_i}{m_e}\right)^{\frac{D+1}{2}}, \tag{A.1}$$

where D is the number of spatial dimensions of the system. Therefore, the rescalings typically operated on m_i/m_e and ω_{pi}/ω_{ci} reduce the computational time by several orders of magnitude.

Magnetic reconnection is a fundamental plasma process that regulates the energization and circulation of plasma in the magnetosphere of the Earth (Dungey 1961) and, to a similar extent, in that of Mercury (Slavin et al. 2010; Dibraccio et al. 2013). The impact of rescaled parameters on magnetic reconnection has been extensively investigated in past numerical works (Shay & Drake 1998; Hesse et al. 1999) that only had access to limited computational resources. There, the authors showed that rescaled parameters only affect the microphysics of the system while leaving the large-scale quantities, such as the reconnection rate, unchanged. Indeed, an increased electron mass impacts the electron distribution function in the electron diffusion region

very locally around the X-point, but leaves the plasma parameters of the outflow unchanged. In particular, electron acceleration by magnetic reconnection is weakly affected by the mass ratio m_i/m_e far from the X-point (Hesse et al. 1999; Haggerty et al. 2015). Magnetic reconnection with guide field is more strongly affected by a reduced ion-to-electron mass ratio (Le et al. 2013), but this is not the case in our simulations, where there is no guide field since the IMF is purely northward or southward. Based on the results of these past works, we expect a negligible impact of the rescaled parameters m_i/m_e and ω_{pi}/ω_{ci} on magnetic reconnection in our simulations of Mercury's magnetosphere.

In the interaction between the solar wind and Mercury's magnetosphere, multiple plasma waves are also excited. In principle, these waves can be affected by the rescalings of m_i/m_e and ω_{pi}/ω_{ci} both in their linear phase and in their corresponding nonlinear dynamics. A comprehensive study of the impact of these rescalings on the nonlinear dynamics of plasma waves is extremely challenging. On the other hand, Verscharen et al. (2020) studied the linear dependence of multiple plasma waves on the parameters m_i/m_e and ω_{pi}/ω_{ci}. There, the authors showed that plasma models with $m_i/m_e \gtrsim 100$ and $\omega_{pi}/\omega_{ci} \gtrsim 10$ (as it is in our case) successfully represents the physics at scales above $\gtrsim 0.2\, d_i$ (which corresponds to $2dx$ in our simulations). Analogous results were obtained by Bret & Dieckmann (2010) studying the impact of m_i/m_e on beam-plasma instabilities. There, the authors concluded that simulations with $m_i/m_e \gtrsim 100$ preserve the hierarchy of the linearly unstable modes and are therefore a good representation of the system.

A.2. Effect of a reduced planet radius

Global fully kinetic simulations of a large system, such as a planetary magnetosphere, are extremely challenging. The large scale separation between the magnetosphere size (at Mercury the magnetopause standoff distance is $d_{MP} \approx 1.5\, R \approx 4 \cdot 10^3$ km) and the ion scale (in the solar wind at Mercury $d_i \approx 50$ km) makes simulations of a real-sized planetary magnetosphere computationally very expensive. The computational time of a simulation with fixed grid resolution, fixed time step, system size $L \sim d_{MP}$, and time $T \sim L/V_{sw}$ scales as:

$$T_{comp} \sim \left(\frac{R}{d_i}\right)^{D+1}, \tag{A.2}$$

where D is the number of spatial dimensions of the system. Therefore, a reduction of the normalized planet radius $R \to \varepsilon R$ reduces the computational time by several orders of magnitude. This rescaling preserves the ratio d_{MP}/R because the magnetic moment of the planet is also reduced by a factor ε^3. In our simulations, we use $\varepsilon = 0.1$ to obtain a reduction in computational time of four orders of magnitude while keeping a good separation between ion kinetic scales (in the solar wind the ion gyroradius is $\rho_i \approx 23$ km) and planetary scales (the reduced planet radius is $R \approx 230$ km).

This rescaling technique was first introduced by Trávníček et al. (2007) for the study of Mercury using global 3D hybrid simulations. There, the authors showed that global simulations using a reduced planet radius (in their case $\varepsilon \approx 0.2$) enable a good representation of the real system and provide useful insight into the global kinetic ion dynamics in the magnetosphere. Further works by those authors using a reduced planet radius have led to important results on the magnetosphere of Mercury in support of MESSENGER observations; see for instance

Trávníček et al. (2009, 2010); Herčík et al. (2013, 2016); Schriver et al. (2011b).

On the one hand, the increased computational power of present HPC facilities (compared to those of 10-15 years ago) has enabled researchers to run global 3D hybrid simulations of Mercury using a real-sized planet (Fatemi et al. 2018; Exner et al. 2018; Aizawa et al. 2020). On the other hand, present state-of-the-art HPC facilities still do not allow global fully-kinetic simulations to be run using a real-sized planet (a computational gap that might be filled in 10-15 years as happened with hybrid simulations). Nonetheless, at present, fully kinetic simulations of the magnetosphere of Mercury are key to planning and interpreting in situ observations by BepiColombo, which is the first mission to address electron scale dynamics at Mercury.

Some authors tried to assess the impact of this planet rescaling on global magnetospheres. Omidi et al. (2004) identified different magnetosphere structures for different values of the normalized magnetopause standoff distance $D_p = d_{MP}/d_i$ using 2D global hybrid simulations. At Mercury, this parameter is of the order of $D_p \sim 1.5~R/d_i \sim 100$. There, the authors found that values $D_p \sim 20$ or greater correspond to an Earth-like magnetosphere structure. Tóth et al. (2017) characterized the minimal rescaling factor ε to run global 3D simulations representative of Earth's magnetosphere using MHD simulations with embedded PIC regions. There, the authors found that, for Earth, a reduction factor of $\varepsilon \gtrsim 1/32$ yields comparable magnetosphere structures and dynamics.

We expect a negligible impact of the planet rescaling on electron adiabatic energization processes. Electrons in the magnetosphere undergo adiabatic betatron and Fermi acceleration while streaming towards the planet and along magnetic field lines, respectively. These processes are well modeled for electrons in our simulations given the large separation between planetary and electron scales (see also the discussion in Lavorenti et al. (2022)). On the contrary, for ions, adiabatic processes can only be poorly modeled in our simulations given the marginal separation between planetary and ion scales in some regions of the scaled-down magnetosphere.

Appendix B: Ion precipitation maps on the surface

Fig. B.1. Ion precipitation maps (same format as Fig. 1) obtained from our fully kinetic simulations. These maps can be used for comparison with other works addressing proton precipitation at Mercury with hybrid models.

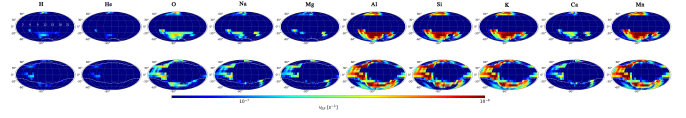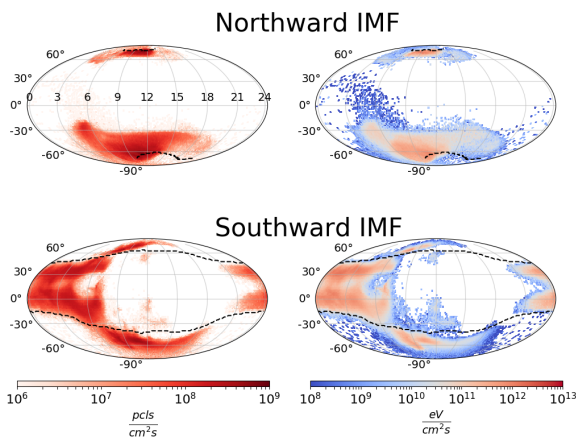## Appendix C: Complete set of EII rate surface maps

Fig. C.1. Full set of EII rates maps (same format as Fig. 2a) for all neutral species considered in this work. These maps are used to build the boxplot in Fig. 2b.